THE ASTROPHYSICAL JOURNAL, 556:872–884, 2001 August 1

PRECIPITATING CONDENSATION CLOUDS IN SUBSTELLAR ATMOSPHERES

ANDREW S. ACKERMAN AND MARK S. MARLEY[1]
NASA Ames Research Center, Moffett Field, CA 94035; ack@sky.arc.nasa.gov, mmarley@mail.arc.nasa.gov
Received 2000 October 26; accepted 2001 March 22

ABSTRACT

We present a method to calculate vertical profiles of particle size distributions in condensation clouds of giant planets and brown dwarfs. The method assumes a balance between turbulent diffusion and sedimentation in horizontally uniform cloud decks. Calculations for the Jovian ammonia cloud are compared with results from previous methods. An adjustable parameter describing the efficiency of sedimentation allows the new model to span the range of predictions made by previous models. Calculations for the Jovian ammonia cloud are consistent with observations. Example calculations are provided for water, silicate, and iron clouds on brown dwarfs and on a cool extrasolar giant planet. We find that precipitating cloud decks naturally account for the characteristic trends seen in the spectra of L- and T-type ultracool dwarfs.

Subject headings: planetary systems — stars: low-mass, brown dwarfs

1. INTRODUCTION

The visual appearance and spectrum of every solar system body with an atmosphere depends strongly on the character and distribution of atmospheric condensates. This is particularly true for the giant planets, for which optically thick cloud decks dominate the appearance of the planets at most continuum wavelengths in both the reflected solar and the thermal infrared. Condensates also play a role in controlling the spectra of at least some brown dwarfs and most extrasolar giant planets. Indeed, one suggested classification scheme (Sudarsky, Burrows, & Pinto 2000) for extrasolar planets hinges on the specific atmospheric condensates present. Yet, despite the importance of condensates, there exists no simple model for predicting the parameters most relevant to radiative transfer: the vertical profile of condensate mass and its distribution over particle size.

Chemical equilibrium models (e.g., Lewis 1969; Fegley & Lodders 1994) predict which species are expected to condense in an atmosphere, yet they provide no guidance as to the expected particle sizes. Other models (e.g., Rossow 1978; Lunine et al. 1989; Carlson, Rossow, & Orton 1988) predict some parameters but lack a simple, self-consistent recipe for exploring the possible phase space in which clouds might exist.

A single example motivates the need for cloud models in substellar atmospheres. With increasingly later spectral type, the warm L dwarfs become progressively redder in their $J-K$ color (e.g., Kirkpatrick et al. 1999; Martín et al. 1999; Fan et al. 2000). Spectral fitting and models (e.g., Leggett, Allard, & Hauschildt 1998; Chabrier et al. 2000; Marley 2000) demonstrate that this is because of the progressive appearance of more silicate dust in the cooling brown dwarf atmospheres. Yet the cooler T-type brown dwarfs, such as Gl 229B, have blue colors in $J-K$ (e.g., Leggett et al. 1999; Tsvetanov et al. 2000). The spectra and colors of these cool brown dwarfs can only be fit by atmosphere models that assume the silicate dust has settled below the visible atmosphere (e.g., Allard et al. 1996; Marley et al. 1996; Tsuji et al. 1996). Models in which the dust does not settle (Chabrier et al. 2000) produce T-dwarf colors that are at least 2 to 3 mag redder than observed. Marley (2000) has demonstrated that a simple model in which all clouds are a single scale-height thick can explain this behavior, but the assumed distribution was prescribed rather than being calculated from any model physics. Correct modeling of the atmospheres of cooling brown dwarfs and the ultimate assignment of an effective temperature scale to the L dwarf spectral sequence (e.g., Kirkpatrick et al. 1999; Basri et al. 2000) requires a characterization of clouds. The ideal model would have a small number of free parameters, predict the vertical distribution and particle sizes of the condensates, and yet be simple enough to be included into model atmosphere codes that iteratively search for self-consistent atmospheric structures. No such ideal model yet exists.

We aim to fill this void by presenting a simple model describing precipitating clouds in substellar atmospheres. We limit our treatment to condensation clouds and, hence, do not consider photochemically driven hazes likely to appear in illuminated stratospheres. We depart from previous work by explicitly treating the downward transport of raindrops with sizes greater than that predicted from the convective velocity scale. Including rainfall produces clouds of thinner vertical extent, which can better reproduce observations of Jupiter's ammonia cloud. The resulting model is general enough to be applied to iron and silicate clouds appearing in brown dwarf atmospheres (e.g., objects with effective temperatures, $T_{\rm eff} \sim 1500$ K) as well as the atmospheres of cool extrasolar giant planets ($T_{\rm eff} \sim 400$ K) in which water clouds dominate the atmosphere. The few free parameters in the model can produce clouds with dramatically different characteristics; ultimately, observations will constrain these parameters and, one hopes, provide information on the underlying atmospheric dynamics and cloud physics.

In this paper, we first summarize previous cloud modeling efforts, then describe the new model. We use the ammonia cloud of Jupiter as a framework for describing the model physics and evaluating the model performance. Finally, we illustrate model applications by considering water, silicate, and iron clouds in the atmospheres of brown dwarfs and a cool extrasolar giant planet.

[1] Department of Astronomy, New Mexico State University, Las Cruces, NM 88003.

2. PREVIOUS MODELS

A great range of models have been used to represent clouds in the terrestrial atmosphere, which vary in the complexity by which atmospheric dynamics and cloud microphysics are treated. The most detailed models simulate three-dimensional cloud-scale motions and resolve the size distributions of cloud droplets (and the aerosols on which they form) and treat the interactions between dynamics, microphysics, and radiative transfer. The computational demands of such complex models limit their domain sizes to a few kilometers in each dimension. Present global-scale (general circulation) models greatly simplify the representation of clouds by parameterizing cloud-scale motions as well as cloud microphysical processes, and such simplifications lead to profound uncertainties in climate predictions from their simulations. Both types of models, as well as a range of intermediate models, can be considered appropriate for modeling the terrestrial atmosphere by virtue of the wealth of observational data available to constrain them; whether or not the unknowns in such models are uniquely constrained by the data constitutes a debate beyond the scope of this study.

The relative scarcity of observational data for clouds in extraterrestrial atmospheres is far less constraining. Leading uncertainties include the characteristics of atmospheric dynamics and the populations of nuclei on which cloud droplets form. Hence, we consider it appropriate to model extraterrestrial clouds using much simpler treatments.

Perhaps the simplest approach to modeling clouds is through a Lagrangian parcel model, in which the base of a cloud appears where the adiabatic cooling of an air parcel in an updraft results in saturation (ignoring any supersaturation associated with barriers to cloud droplet formation). Further cooling condenses vapor in excess of saturation onto cloud particles. The particles grow through condensation and coalescence until their sedimentation velocities exceed the updraft speed and then fall out of the parcel. A number of problems arise in the formulation of updraft parcel models, among them: ignoring parcels in downdrafts, treating the mixing between parcels, treating the source of condensates into a parcel caused by sedimentation from above, and determining updraft speeds.

Another simple approach, which we employ here, is through a one-dimensional Eulerian framework, in which turbulent diffusion mixes a condensable vapor upward, while maintaining a constant mixing ratio (equivalently, mole fraction) below the cloud. Temperature and, hence, the saturation mixing ratio in the air column decrease with altitude, and the cloud base again appears where the saturation mixing ratio matches the subcloud mixing ratio. Above the cloud base, turbulent diffusion works toward maintaining a constant total mixing ratio ($q_t = q_v + q_c$), which is the sum of the vapor (q_v = moles of vapor per mole of atmosphere) and condensate (q_c = moles of condensate per mole of atmosphere) mixing ratios, while sedimentation reduces q_t by transporting condensate downward. Note that by ignoring horizontal variability, any differences between (cloudy) updrafts and (potentially cloud-free) downdrafts are neglected.

A number of models for tropospheric condensation clouds have appeared in the planetary and astrophysical literature. Here we summarize a selection of them that contribute to the present work.

2.1. *Lewis* (1969)

Lewis (1969) represents a foundation in the study of tropospheric clouds in the giant planets. In that work, the term "precipitation" is used in the narrow sense used by chemists, in which condensates appear where the local saturation vapor pressure is exceeded by the actual vapor pressure rather than in the broader sense employed by meteorologists, which additionally denotes sedimentation of the condensates (hereafter we use the term in this broader sense). Although there is no mention of sedimentation by Lewis, the treatment does imply certain assumptions. Starting below the cloud base and working upward, at each computational level the Lewis model assumes that all the condensate remains at the level where it appears. Considered in the framework of a parcel in an updraft, the Lewis model assumes that all condensate rains out with a fallspeed matching the updraft velocity. Were sedimentation slower, condensate would be transported upward (as discussed by Weidenschilling & Lewis 1973); were sedimentation faster, condensate would be transported downward. Hence, the Lewis (1969) assumption regarding sedimentation is an unstated compromise between those two possibilities.

We implement the Lewis model by starting below the cloud base (where $q_c = 0$ and $q_v = q_{\text{below}}$) and condensing all vapor in excess of saturation at each successive level upward:

$$q_c(z) = \max\,[0,\, q_v(z - \Delta z) - q_s(z)]\,, \tag{1}$$

$$q_v(z) = \min\,[q_v(z - \Delta z),\, q_s(z)]\,, \tag{2}$$

where z is altitude and q_s is the vapor mole fraction corresponding to the saturation vapor pressure at that altitude. The first and second cases on the right-hand side correspond to cloud-free and cloudy conditions, respectively. Note that under all conditions $q_t(z) = q_v(z - \Delta z)$ in the Lewis model, reflecting the assumption that only vapor is transported upward.

Beyond this simple model, Lewis (1969) considered the partitioning of chemical species in some detail and also calculated pseudo-adiabatic lapse rates. Here we simply assume that each condensate results from the saturation of a single condensable and fix the lapse rate as input from observations or an external model.

For an example, we calculate an ammonia cloud profile from the Lewis model (Fig. 1) using the Jovian temperature profile from *Voyager* (Lindal et al. 1981), the relation for vapor pressure given in Appendix A, and a subcloud mole fraction of 3×10^{-5} (a wide range of abundances below the expected base of the Jovian ammonia cloud have been reported; we adopt the value at 0.6 bars retrieved by Kunde et al. [1982] for the Northern Equatorial Belt, which also agrees with the best-fit values of Carlson, Lacis, & Rossow [1993] and Brooke et al. [1998]). The cloud base appears at 0.42 bars, where the temperature is 129 K. Although absent in the figures of Lewis (1969; likely caused by reduced vertical resolution), in our interpretation of that model, the vapor is not entirely depleted in the lowest reaches of the cloud (where $q_c < q_t$); hence, q_c increases above the cloud base. Such an increase is found in terrestrial clouds of moderate vertical extent, where $q_c < q_t$, and hence q_c increases with altitude throughout their depths. However, at greater altitudes in this deep ammonia cloud, the vapor is so effectively depleted by condensation at the low temperatures

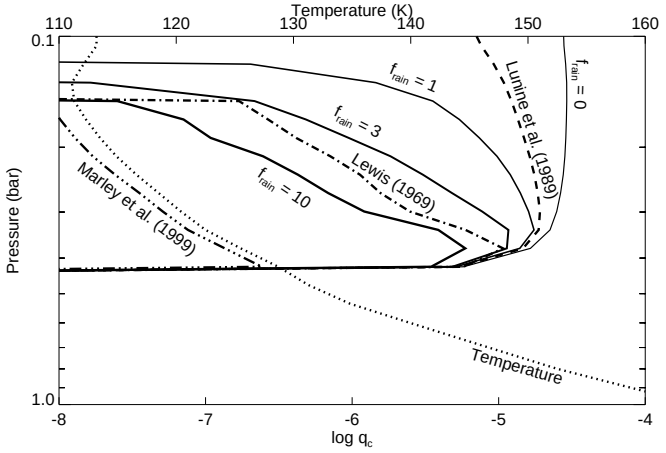

FIG. 1.—Vertical profiles of mole fraction (mixing ratio by volume) of condensed ammonia (q_c) from the present model of Jovian ammonia cloud with different values $f_{\rm rain}$ and from our adaptations of other models as labeled. The vertical coordinate is atmospheric pressure. The dotted line is the temperature profile. The kinks in the condensate profiles are caused by ripples in the temperature profile.

that $q_v \ll q_t$, leading to a cold degeneracy, $q_c(z) \approx q_t(z) = q_s(z - \Delta z)$, in which decreasing temperatures result in q_c diminishing with altitude. Note that the condensate abundance drops off rapidly above $\sim$0.13 bars because of increasing temperatures. Hence, the temperature minimum quite reasonably produces a cold trap in the Lewis model.

Condensate particle sizes, the other ingredient needed for predicting cloud opacity, are not considered by Lewis (1969) or Weidenschilling & Lewis (1973).

2.2. *Carlson et al.* (1988)

In their theoretical characterization of cloud microphysics of the giant planets, Carlson et al. (1988) employ the formalism of Rossow (1978) to calculate time constants for droplet condensation within cloudy updrafts (assuming a supersaturation of 10^{-3}), droplet coalescence (assuming the mean collision rate is described by particles with a mass ratio of 2), and sedimentation through an atmospheric scale height. From these time constants, estimates are made of the predominant size of cloud particles at cloud base for a number of condensates. For the Jovian ammonia cloud, Carlson et al. estimate a mass-weighted droplet radius of $\sim$10–30 μm.

Carlson et al. (1988) make no attempt to calculate vertical profiles of condensate mass. For profiles of vapors that condense into multiple forms (such as ammonia, which can also condense onto a cloud of NH_4SH below the ammonia cloud), saturation is assumed above the cloud base.

A shortcoming to the approach of Carlson et al. (1988) is that their microphysical time constants strongly depend on a number of uncertain factors, chief among them completely unknown supersaturations, which govern droplet growth rates caused by condensation. Supersaturations in a cloudy updraft are determined by balance between the source caused by adiabatic cooling and the sink caused by condensation. Uncertainties in updraft speeds and the populations of condensation nuclei (and hence cloud droplets) both contribute to the uncertainty in supersaturations realized in extraterrestrial clouds. Furthermore, the time constants Carlson et al. (1988) use for gravitational coalescence assume that the collection efficiency is unity, and those for sedimentation effectively assume a fixed width of the size distribution. Rather than attempting to constrain the many degrees of freedom using such a detailed approach, we choose instead to reduce the number of assumptions by simplifying the description of cloud microphysics.

2.3. *Lunine et al.* (1989)

Lunine et al. (1989) consider a range of possible iron and silicate clouds in brown dwarfs; the possibilities differ in the nature of the balance between sedimentation and turbulent mixing. The framework is based on a theoretical investigation into iron clouds deep in the Jovian atmosphere by Prinn & Olaguer (1981), which in turn draws on an analysis of sulfuric acid clouds on Venus (Prinn 1974). These models represent a fleshing out of the discussion of vertical transport of condensates by Weidenschilling & Lewis (1973).

Two fundamental cloud types are treated by Lunine et al. (1989). The first is "dustlike" (using the terminology of Prinn & Olaguer 1981), in which cloud particles grow and efficiently sediment out, resulting in relatively thin clouds limited by the local vapor pressure, as in the model of Lewis (1969). These dustlike clouds are assumed to prevail in the radiative region (stratosphere), where the temperature profile is stable and convection is suppressed.

The second fundamental type in the Lunine et al. (1989) study is a tropospheric cloud, in which downward transport by sedimentation opposes upward transport by turbulent mixing. For this cloud type, two variations are considered by Lunine et al. (1989). For the first variation, described as "frozen-in," cloud particles are so small that sedimentation is overwhelmed by upward transport caused by turbulent mixing. In this case, the atmosphere is well mixed with respect to condensate; hence, q_c is independent of altitude above the cloud base. For the second variation, which is intermediate to the dustlike and frozen-in cases, particles grow large enough in "convective" clouds to develop appreciable sedimentation velocities, and their downward sedimentation is balanced by their turbulent transport upward. For their calculations of specific brown dwarf models, Lunine et al. (1989) consider only the two endmembers of their cloud spectrum, corresponding to dustlike and frozen-in clouds.

Their intermediate case serves as a starting point for our model of condensate mass profiles. Our interpretation of the convective cloud model of Lunine et al. (1989) as applied to the Jovian ammonia cloud is shown in Figure 1. Note that we have refined that model slightly, allowing the atmospheric properties to vary with height above the cloud base and relaxing their assumption that $q_c = q_t$. The condensate mass is seen to be significantly enhanced above the cloud base for that model: at the tropopause (where there is no cold trap in this case) q_c is enhanced a thousandfold over that computed by the Lewis (1969) model. Thus, the treatment in which Lunine et al. (1989) assume particle sedimentation to balance turbulent transport results in a cloud not so different from their frozen-in case (as depicted by the curve in Fig. 1 labeled $f_{\rm rain} = 0$). Evidently, the sedimentation in this convective cloud model is far less effective than that assumed by Lewis (1969). As described below, for our calculations of condensate mass profiles, we extend the Lunine et al. (1989) approach by applying a scale factor to the particle sedimentation.

For radiative calculations, Lunine et al. (1989) assume all particles in the frozen-in and dustlike clouds are 1 and 10 μm in radius, respectively.

2.4. *Marley et al.* (1999)

The Marley et al. (1999) model of water and silicate clouds in extrasolar giant planets represents a variation on the Lewis (1969) model. As in the Lewis model, the calculation of vapor pressure (or, equivalently, q_v) assumes that any supersaturation is quenched locally by condensation (eq. [2]). However, the calculation of the condensate mole fraction (q_c) represents a departure: instead of calculating it from the vapor pressure in the underlying layer from equation (1), Marley et al. scale it to the local saturation vapor pressure with the following assumption:

$$q_c(z) = \begin{cases} 0 & \text{if } q_v(z - \Delta z) < q_s(z), \\ f_s\, q_s(z) & \text{otherwise.} \end{cases} \quad (3)$$

The parameter f_s corresponds to the potential supersaturation prior to condensation. Marley et al. (1999) treat f_s as an adjustable parameter, ranging from a baseline value of 0.01 to an extreme value of 1. The baseline model as applied to the Jovian ammonia cloud is shown in Figure 1. The condensate mass is seen to be diminished by a factor of ~ 100 relative to the Lewis (1969) model.

Increasing f_s to 1 results in a hundredfold enhancement of q_c throughout the cloud in comparison with that of the baseline case, as shown in Figure 2*a*. The principle difference between that extreme and the Lewis (1969) condensate model is that for the former there is no regime near the cloud base akin to shallow terrestrial clouds, in which q_c increases with altitude. This difference is attributable to a discontinuity of q_t in the treatment of Marley et al.: below the cloud base $q_t(z) = q_v(z - \Delta z)$, as in the Lewis (1969) model, but above the cloud base, $q_t(z) = (1 + f_s)q_s(z)$.

For their calculations of cloud particle sizes, which are decoupled from their calculation of condensate mass, Marley et al. (1999) apply the formalism of Rossow (1978) to two atmospheric endmembers: first, a quiescent atmosphere, in which the mean particle size is determined from the condition that the sedimentation rate matches the faster of coagulation and condensation (at an assumed supersaturation of 0.01); and, second, a turbulent atmosphere in which mixing is balanced by sedimentation.

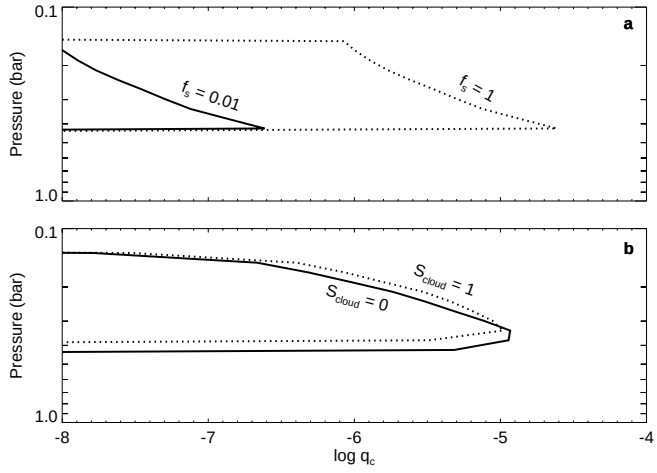

FIG. 2.—Vertical profiles of condensed ammonia (as in Fig. 1) from (*a*) the model of Marley et al. (1999) for two values of f_s (the potential supersaturation prior to condensation) and from (*b*), our baseline model for two comparable values of $S_{\rm cloud}$ (the supersaturation persisting after condensation).

The first endmember is subject to a similar catalog of unconstrained assumptions as required by the treatment of Carlson et al. (1988), the most notable among them being the great uncertainty in the supersaturation driving droplet condensation. Also, the model physics underlying this quiescent atmosphere seems to be self-contradictory—on the one hand explicitly assuming that there is too little convection to regulate the maximum size of the droplets, yet on the other hand implicitly assuming that there is enough convection to supply the vapor necessary to drive condensational growth.

However, the second case of Marley et al. (1999) requires significantly fewer assumptions and is also appropriate to tropospheric condensation clouds. This second case serves as a starting point for the calculation of the cloud particle sizes in our model.

3. THE PRESENT MODEL

We model all condensation clouds as horizontally homogeneous (globally averaged) structures, the vertical extent of which is governed by a balance between the upward turbulent mixing of condensate and vapor ($q_t = q_c + q_v$) and the downward transport of condensate caused by sedimentation:

$$-K\,\frac{\partial q_t}{\partial z} - f_{\rm rain}\, w_*\, q_c = 0\,, \quad (4)$$

where K is the vertical eddy diffusion coefficient and $f_{\rm rain}$ is a new parameter we have introduced, defined as the ratio of the mass-weighted droplet sedimentation velocity to w_*, the convective velocity scale. We solve equation (4) for each condensate independently and, hence, ignore any microphysical interactions between clouds. Equation (4) is an extension of Lunine et al.'s convective cloud model, relaxing their implicit assumptions $f_{\rm rain} = 1$ and $q_c = q_t$.

The product $f_{\rm rain}\, w_*$ represents an average sedimentation velocity for the condensate, which offsets turbulent mixing and thereby leads to q_t decreasing with altitude. The extreme case with no sedimentation to offset turbulent mixing ($f_{\rm rain} = 0$) is equivalent to the frozen-in endmember of Lunine et al. (1989) and the "dusty" models of the Lyon group (e.g., Chabrier et al. 2000). In this case, the solution to equation (4) is a well-mixed atmosphere (q_t independent of altitude), which is seen in Figure 1 to loft even more condensate than the convective cloud of Lunine et al. (1989).

We adopt $f_{\rm rain}$ as an adjustable input parameter, which together with q_c constrains the droplet size distributions. First we describe our calculation of q_c, then the size distributions.

3.1. *Condensate Mass Profiles*

The eddy diffusion coefficient (K) for q_t is assumed to be the same as that for heat as derived for free convection (Gierasch & Conrath 1985):

$$K = \frac{H}{3}\left(\frac{L}{H}\right)^{4/3}\left(\frac{RF}{\mu\rho_a\, c_p}\right)^{1/3}\,, \quad (5)$$

where the atmospheric scale height is given by $H = RT/\mu g$ (for Jupiter, we use $g = 25$ m s^{-2}), L is the turbulent mixing length, R the universal gas constant, μ the atmospheric molecular weight (2.2 g mol^{-1} assumed here), ρ_a the atmospheric density, and c_p the specific heat of the atmosphere at constant pressure (ideal gas assumed). Here we assume all

the interior heat to be transported through the convective heat flux: $F = \sigma T_{\rm eff}^4$, where σ is the Stefan-Boltzmann constant and the effective temperature for Jupiter is $T_{\rm eff} = 124$ K. In the general case, a profile of F is specified by an external model, which partitions the transport of interior heat between radiative and convective fluxes. The convective heat flux can be reduced further by other heat fluxes, such as para-hydrogen conversion or latent heat release, as discussed by Gierasch & Conrath (1985). Beyond any uncertainty in the convective heat flux, the constant coefficient scaling the eddy diffusion coefficient is only loosely constrained by observations. For our baseline model, we use a coefficient of $\frac{1}{3}$ based on previous modeling studies of the Jovian atmosphere (D. M. Hunten 1996, private communication) and consider the sensitivity of our model results to its value in a subsequent section.

For freely convecting atmospheres, the mixing length is typically assumed to be the pressure scale height. However, in stable atmospheric regions, the mixing length will be diminished. We account for this reduction by scaling the mixing length to the local stability:

$$L = H \max (\Lambda, \Gamma/\Gamma_{\rm adiab}) , \quad (6)$$

where Γ and $\Gamma_{\rm adiab}$ are the local and dry adiabatic lapse rates, respectively, and Λ is the minimum scaling applied to L (we assume a value of 0.1). In the general case, convective heat fluxes are diminished in radiative regions; hence, we also assume an eddy diffusion coefficient no less than a prescribed minimum value ($K_{\rm min} = 10^5$ cm^2 s^{-1} in our baseline model), which represents residual turbulence caused by breaking buoyancy waves (Lindzen 1981) and such. A list of prescribed/adjustable parameters is provided in Table 1.

The remaining parameter in equation (5) is the convective velocity scale from mixing-length theory: $w_* = K/L$. Our baseline values for the turbulent mixing parameters just below the Jovian ammonia cloud are $H = L = 20$ km, $K = 2 \times 10^8$ cm^2 s^{-1}, and $w_* = 1$ m s^{-1}.

To compute the vertical distributions of condensate and vapor, we proceed upward from the subcloud conditions, requiring all excess vapor to condense and solving equation (4) at each level. If we heuristically assume that q_c/q_t and L are constant in a cloud, the solution is an exponential decline of total mixing ratio with height above cloud base (where we define $z = 0$):

$$q_t(z) = q_{\rm below} \exp \left(-f_{\rm rain} \frac{q_c}{q_t} \frac{z}{L} \right) . \quad (7)$$

Note that by using the subcloud mixing ratio as a lower boundary condition, any moistening caused by rain evaporating below the cloud base is ignored.

Comparing our adaptation of the Lunine et al. (1989) profile with our calculation using $f_{\rm rain} = 1$ isolates the effect of reducing the mixing length caused by atmospheric stability. The cumulative effect of the progressive reduction in mixing length because of the stability of the *Voyager* temperature profile above the cloud base is seen to result in a cold trap in the lower stratosphere. Tripling $f_{\rm rain}$ further reduces the cloud density and lowers the cold trap to the tropopause; increasing it to 10 results in a cloud with less condensate than the Lewis (1969) model.

We assume that $f_{\rm rain}$ is independent of altitude. Yet specifying an appropriate value of $f_{\rm rain}$ at the cloud base, let alone any vertical dependence, poses a significant challenge. For guidance, first we turn to in situ measurements and detailed simulations of terrestrial water clouds and then consider constraints provided by values retrieved through remote sensing of Jovian ammonia clouds.

For terrestrial stratocumulus clouds capping well-mixed planetary boundary layers, we find that $f_{\rm rain} < 1$ in the cloud deck and increases with distance below cloud top. An assortment of in situ measurements indicates that $f_{\rm rain}$ increases with decreasing droplet concentrations (N), as fewer and, hence, larger droplets more efficiently produce drizzle and thereby decrease cloud water. For example, $f_{\rm rain} \sim 0.2$ for a case study over the North Sea, where $N = 100$ cm^{-3} (Nicholls 1984), while in California stratocumulus it increased from 0.3 to 0.5 as N decreased from 40 cm^{-3} in clouds contaminated by ship exhaust to 10 cm^{-3} in clean ambient air (from Fig. 3*b* of Ackerman et al. 2000b). We note that in clean marine stratocumulus, reduced rain is observed (e.g., Taylor & Ackerman 1999) and predicted (e.g., Ackerman, Toon, & Hobbs 1993; Stevens et al. 1998) to result in deeper cloud layers, which is consistent with our simple model. However, any changes in cloud cover associated with precipitation changes are not represented in our model.

We have also calculated profiles of $f_{\rm rain}$ for deeper convection, using large-eddy simulations of trade cumulus clouds (Ackerman et al. 2000a), which are twice as deep as stratocumulus clouds ($\sim$1000 m compared to $\sim$500 m). As in the stratocumulus clouds, we find that $f_{\rm rain} < 1$ in the stratiform anvils at cloud top. However, $f_{\rm rain}$ is significantly enhanced throughout the bulk of the trade cumulus clouds, where it ranges from $\sim$2 to 6. Vertical winds are more symmetrically distributed in stratocumulus; hence, the convective velocity scale is representative of the mean updraft velocity. The circulation is more skewed in trade cumulus, with narrow updrafts opposing the broad subsidence: for the Ackerman et al. (2000a) trade-cumulus simulations, the mean vertical velocity in cloudy updrafts is three times the convective velocity scale. Such a skewness is consistent with an enhancement of the rain factor in deep convection.

We recommend a more systematic analysis of $f_{\rm rain}$ in terrestrial clouds. Perhaps more pertinent to the much deeper clouds expected in gas giants and brown dwarfs, we also

TABLE 1

ADJUSTABLE MODEL PARAMETERS

Parameter	Baseline Value	Description
$f_{\rm rain}$	3	Ratio of mass-weighted sedimentation velocity to convective velocity scale
$K_{\rm min}$	10^5 cm^2 s^{-1}	Minimum value of eddy diffusion coefficient
Λ	0.1	Minimum ratio of turbulent mixing length to atmospheric scale height
$S_{\rm cloud}$	0	Supersaturation that persists after accounting for condensation
σ_g	2	Geometric standard deviation in lognormal size distributions of condensates

recommend consideration of much deeper convection than considered here. For now, we treat $f_{\rm rain}$ as an adjustable parameter, leaning toward values greater than 1, as we expect the deep convection in substellar atmospheres (on the order of an atmospheric scale height and deeper) to more closely resemble cumuliform than stratiform convection in the terrestrial atmosphere.

For observations of Jovian ammonia clouds, we first turn to the retrievals obtained from the *Voyager* IRIS (Infrared Interferometer Spectrometer) instrument by Carlson, Lacis, & Rossow (1994), who considered latitudinal variations among zones and belts in the Jovian tropics. Although they did not provide profiles of condensed ammonia, we can compare our results to their ratios of condensate to atmospheric scale height (H_p/H_g in their notation). Carlson et al. (1994) retrieve ratios of 0.35 and 0.40 (± 0.10) for ammonia clouds in the Equatorial and Northern Tropical Zones, respectively, which are seen in Figure 3 to span a range of $f_{\rm rain}$ values between ~ 1 and 3. Retrievals of ammonia cloud properties for the Jovian tropics from *ISO* (Infrared Space Observatory) measurements by Brooke et al. (1998) indicate a scale height ratio of 0.3, which is consistent with our model results for $f_{\rm rain} \sim 2$.

Were the ratio q_c/q_t fixed in our model, as assumed heuristically for equation (7), the condensate height should vary as $f_{\rm rain}^{-1}$. However, as seen in Figure 3, the model dependence is not nearly that steep, and for $f_{\rm rain} > 3$ the dependence nearly vanishes. The dependence is moderated by a negative feedback in which q_c/q_t decreases with increasing $f_{\rm rain}$. Our assumption of zero supersaturation within a cloud is equivalent to $q_c/q_t = S - 1$, where S is the potential supersaturation before condensation eliminates it. Increased $f_{\rm rain}$ offsets more of the turbulent mixing of vapor and condensate, thereby reducing the potential supersaturation and decreasing the ratio q_c/q_t. The negative feedback is thereby caused by the reduction of q_c/q_t, which diminishes the dependence of the condensate scale height on $f_{\rm rain}$ (eq. [7]).

The assumption that all vapor in excess of saturation condenses can be relaxed in our model by replacing equation (1) with

$$q_c(z) = \max\,[0,\, q_v(z - \Delta z) - (S_{\rm cloud} + 1)q_s(z)]\,, \qquad (8)$$

where $S_{\rm cloud}$ is the supersaturation that persists after accounting for condensation. Allowing $S_{\rm cloud} > 0$ represents conditions in which there is a significant barrier to the formation of cloud droplets and/or condensation is too slow to effectively offset the supersaturation driven by cooling in updrafts. In shallow terrestrial water clouds, such as stratocumulus, neither of these conditions holds, as there are typically abundant condensation nuclei upon which droplets form at low supersaturations and the concentration and diffusivity of water vapor are sufficient to allow condensation to balance the modest dynamic forcing at low supersaturations ($\sim 10^{-3}$). However, in cirrus clouds that form directly from the vapor phase (as opposed to the freezing of water droplets from deep convection), there are typically few effective ice nuclei available; hence, the barrier to nucleation can result in supersaturation building to ~ 0.5 before ice crystals form, even in moderate updrafts. High supersaturations (~ 0.3) can be maintained after nucleation in cirrus clouds because the concentration and diffusivity of water vapor are greatly reduced at the cold temperatures of the upper troposphere (Jensen et al. 2000).

As extreme cases, in Figure 2*b* the condensate profile for $S_{\rm cloud} = 0$ is compared to that for $S_{\rm cloud} = 1$. The barrier to condensation results in a lifting of the cloud base and enhanced lofting of vapor, but the altitude of the cold trap is unchanged (recall that the temperature profile is fixed here). The greater lofting enhances condensate mass above ~ 0.4 bar, which tends to increase the column of condensate. However, the tendency is more than offset by the decrease in atmospheric mass density at the elevated cloud base; hence, the condensate column decreases from 52 to 39 g m^{-2} in response to increasing $S_{\rm cloud}$ from 0 to 1. This 25% reduction of condensate column contrasts markedly with the effect of increasing f_s from 0.01 to 1 in the Marley et al. (1999) model, in which the condensate column increases a hundredfold (Fig. 2*a*). These opposite responses (to comparable changes in maximum relative humidities: from 100% to 200% for the present model and from 100.01% to 200% for the Marley et al. model) arise from the distinct definitions of the supersaturation factor: $S_{\rm cloud}$ corresponds to the supersaturation *after* condensation is treated in the present model, whereas f_s corresponds to the potential supersaturation *before* condensation is treated in the Marley et al. model. Marley et al.'s f_s is more comparable to $f_{\rm rain}^{-1}$ than to $S_{\rm cloud}$ in the present model.

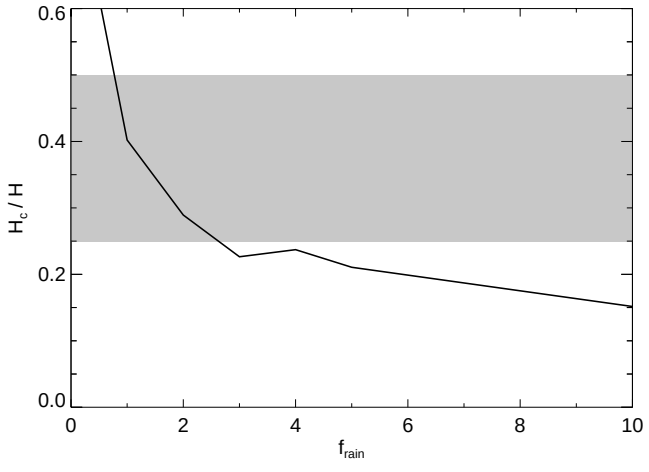

FIG. 3.—Ratio of the condensed ammonia scale height to the atmospheric pressure scale height (H_c and H, respectively) as a function of $f_{\rm rain}$. The model condensate scale height is calculated from the altitude of the peak opacity (for geometric scatterers) and the altitude at which the opacity falls to exp(-1) of its peak. The gray region depicts the range of scale height ratios retrieved from the Jovian Equatorial and Northern Tropical Zones by Carlson et al. (1994).

3.2. *Droplet Size Distributions*

Size spectra of cloud particles in terrestrial condensation clouds are commonly observed as bimodal number distributions, with a condensational mode of radius ~ 10 μm (for liquid clouds) resulting from condensational growth at modest supersaturations and a precipitation mode at larger radii resulting from coalescence driven by dispersion in sedimentation velocities. The bimodal structure is evident in cloud droplet size distributions measured in stratocumulus off the coast of California, as shown in Figure 4*a*. At the cloud base, the mean size of the condensation mode depends on factors such as the updraft velocity and the composition and size distribution of the condensation nuclei upon which droplets form. Above the cloud base, the mean size of the condensation mode increases with altitude in an updraft.

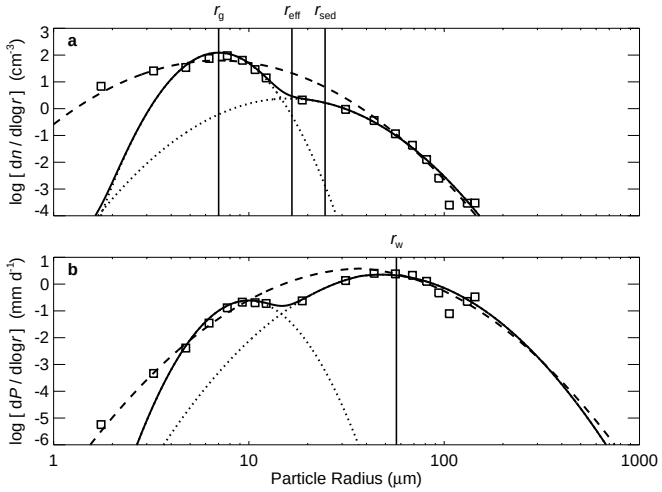

FIG. 4.—Measured size distributions (squares) of (*a*) cloud droplet number concentration (*n*, in cm^{-3}) and (*b*) precipitation flux (*P*, in mm d^{-1}) measured in California stratocumulus and averaged over 12 km of flight at 200 m altitude, ~100 m below cloud top (from Fig. 3*b* of Ackerman et al. 2000b). The solid curve is a bimodal fit to the measurements, the sum of two lognormal distributions (*dotted curves*). The dashed curve is a monomodal lognormal fit to the measurements, in which $N = 40$ cm^{-3}, $r_g = 7$ μm, and $\sigma_g = 1.8$ (symbols defined in text). The values of r_g, $r_{\rm eff}$, and $r_{\rm sed}$ are tied to the monomodal fit to the measurements, while r_w is calculated from the convective velocity, measured to be 0.33 m s^{-1} (I. Brooks 1995, private communication).

The production of precipitation in terrestrial clouds is generally observed to increase with the mean size and spectral width of the condensation mode. The mean size of droplets in the precipitation mode[2] is found to increase with distance from cloud top in marine stratocumulus (e.g., Nicholls 1984) (the opposite tendency of the condensation mode), typically explained in microphysical terms as caused by "fortunate" collector drops sweeping up smaller droplets and growing as they fall. Such a profile is consistent, as it must be, with the observed decrease in $f_{\rm rain}$ with height above the cloud base. We note in passing that measured profiles of $f_{\rm rain}$ in shallow convection are also consistent with our assumption that the size of precipitation particles decreases as convective velocity decreases above the cloud base, though we assume a uniform value of $f_{\rm rain}$ in our model calculations.

We make no attempt to model the complexity of cloud processes here, as such detailed computations are prohibitively demanding, and the parameter space of unknowns is overwhelming for the range of condensates expected in substellar atmospheres (including such basic issues as whether condensates are solid or liquid). Instead, we simply prescribe a single, broad lognormal size distribution of condensate particles at each level (Fig. 4), thereby halving the number of parameters required for a bimodal distribution. The lognormal size distribution is given by

$$\frac{dn}{dr} = \frac{N}{r\sqrt{2\pi}\ln\sigma_g}\exp\left[-\frac{\ln^2(r/r_g)}{2\ln^2\sigma_g}\right], \tag{9}$$

where n is the number concentration of particles smaller than radius r, and the three parameters to be constrained appear on the right side: N is the total number concentration of particles, r_g the geometric mean radius, and σ_g the geometric standard deviation.

Marley et al. (1999) also prescribe a lognormal size distribution of condensate particles, in which σ_g is fixed at 1.5 and r_g is determined from the particle sedimentation velocity corresponding to the convective velocity scale (w_*). We choose to use σ_g as an adjustable parameter and determine N and r_g through q_c and $f_{\rm rain}$. The rain factor is rigorously defined through

$$f_{\rm rain} = \frac{\int_0^\infty v_f(dm/dr)dr}{\epsilon\rho_a w_* q_c}, \tag{10}$$

where v_f is the particle sedimentation velocity (described in Appendix B), m is particle mass, and ϵ is the ratio of condensate to atmospheric molecular weights. To close the system analytically, we fit a power-law dependence for particle fallspeed about its value at $v_f(r_w) = w_*$ through

$$v_f = w_*(r/r_w)^\alpha, \tag{11}$$

where the exponent α is calculated from a fit to the fallspeeds between r_w/σ and r_w when $f_{\rm rain} > 1$ and between r_w and $r_w\,\sigma$ otherwise (σ is constrained to be ≥ 1.1 for the fit). The power-law approximation allows equation (10) to be expressed as

$$f_{\rm rain} = \frac{\int_0^\infty r^{3+\alpha}(dn/dr)dr}{r_w^\alpha\int_0^\infty r^3(dn/dr)dr}. \tag{12}$$

Integration of the lognormal distribution then leads to

$$r_g = r_w\, f_{\rm rain}^{1/\alpha}\exp\left(-\frac{\alpha+6}{2}\ln^2\sigma_g\right), \tag{13}$$

$$N = \frac{3\epsilon\rho_a q_c}{4\pi\rho_p r_g^3}\exp\left(-\frac{9}{2}\ln^2\sigma_g\right), \tag{14}$$

where ρ_p is the density of a condensed particle (see Appendix B). The parameter $f_{\rm rain}$ can be interpreted in terms of microphysics by identifying the radius of mass-weighted sedimentation flux in equation (12):

$$r_{\rm sed} = \left[\frac{\int_0^\infty r^{3+\alpha}(dn/dr)dr}{\int_0^\infty r^3(dn/dr)dr}\right]^{1/\alpha}, \tag{15}$$

which leads to $f_{\rm rain} = (r_{\rm sed}/r_w)^\alpha$. In Figure 4*b*, the size distribution is weighted by precipitation, where it is seen that $r_{\rm sed} < r_w$, consistent with $f_{\rm rain} < 1$. In contrast, for the large-eddy simulations of trade cumulus mentioned above, and as implied by the retrievals from the Jovian ammonia clouds, the droplets grows sufficiently large to satisfy $r_{\rm sed} > r_w$.

It is seen from equations (12)–(14) that droplet sizes are decoupled from condensate mass (though both depend on $f_{\rm rain}$); the condensate mass simply scales the distribution through N. Ignoring any vertical dependence of atmospheric stability (eq. [6]), vertical variations in droplet sizes are caused by the height dependence of convective velocity, leading to $r_w \propto \rho_a^{1/3\alpha}$, which yields a mild vertical dependence of approximately $r_w \propto \rho_a^{1/4}$ for our baseline Jovian ammonia cloud (for which $\alpha = 1.3$, corresponding to a moderately turbulent sedimentation regime in which fallspeeds are reduced from those in viscous flow).

Of greater interest than the mild vertical dependence are the sensitivities of droplet sizes on $f_{\rm rain}$ and σ_g at the base of

[2] The maximum size of precipitation particles is set by their breakup because of hydrodynamic instability, which for terrestrial raindrops occurs at a radius of ~3 mm.

our Jovian ammonia cloud, where $r_w = 35$ μm. For a given value of σ_g, more efficient rain implies larger droplets: $r_g \propto f_{\rm rain}^{1/\alpha}$. For our baseline droplet distribution (with $\sigma_g = 2$), a value of $f_{\rm rain} = 3$ leads to $r_g = 14$ μm (compare to ~ 10 μm for shallow terrestrial clouds), while $f_{\rm rain} = 5$ yields $r_g = 20$ μm.

For efficient precipitation ($f_{\rm rain} > 1$), reducing the width of the size distribution requires an increase in r_g, as the narrower distribution is centered on a larger radius. For example, a monodisperse distribution ($\sigma_g = 1$) with $f_{\rm rain} = 3$ results in $r_g = 77$ μm. Such narrow distributions of large particles could result from condensational growth at high supersaturations, reminiscent of methane "rain without clouds" suggested by Toon et al. (1988) for Titan's atmosphere.

In the complete model, we calculate spectrally resolved profiles of condensate opacity by integrating the scattering and absorption coefficients (from Mie calculations) over the particle size distributions. Here we simply present opacities for geometric scatterers, which for a model layer of thickness Δz is given by

$$\Delta\tau = \frac{3}{2}\frac{\epsilon\rho_a q_c}{\rho_p r_{\rm eff}}\Delta z\ , \tag{16}$$

where the effective (area-weighted) droplet radius is evaluated from the lognormal size distribution:

$$r_{\rm eff} = r_w\, f_{\rm rain}^{1/\alpha} \exp\left(-\frac{\alpha+1}{2}\ln^2\sigma_g\right). \tag{17}$$

The effective radius can be greater or less than r_w, depending on the combination of $f_{\rm rain}$, α, and σ_g. At the base of our baseline Jovian ammonia cloud $r_{\rm eff} = 46$ μm, which is 11 μm greater than r_w.

The computation of cloud optical depth depends on vertical grid resolution caused by the exponential temperature dependence of saturation vapor pressures. To reduce such resolution dependence, we progressively subdivide each model layer until its optical depth converges to 1% precision. For the Jovian ammonia cloud, our calculations converge at a minimum sublayer thickness of ~ 30 m.

Equations (16) and (17) show that increased precipitation reduces opacity not only by decreasing q_c but also by increasing $r_{\rm eff}$. For heuristic purposes, the column optical depth can be estimated from the cloud base properties by ignoring any height dependence of the mixing length and atmospheric scale height and assuming $q_c = q_t$ within the cloud, in which case

$$\tau = \frac{3}{2}\frac{\epsilon p q_{\rm below}}{g r_{\rm eff}(1+f_{\rm rain})}\ , \tag{18}$$

where p and $r_{\rm eff}$ are atmospheric pressure and droplet effective radius at the cloud base. Note that τ is more than linearly dependent on $q_{\rm below}$ because of its dependence on the cloud base pressure. For the following comparisons with observations of the Jovian ammonia cloud, we sum optical depths from equation (16) over the model layers and compute a cloud average $r_{\rm eff}$ from the cloud optical depth and vertical column of condensate.

4. COMPARISONS WITH OBSERVATIONS

West, Strobel, & Tomasko (1986) attempt to reconcile among a vast array of observations of the Jovian ammonia cloud and conclude that its optical depth at visible wavelengths is between ~ 2 and 10, made up of a population of small particles ($r \sim 1$ μm) reaching the tropopause in both belts and zones, underlain in zones by a population of larger particles ($r \sim 3$–100 μm) concentrated near the cloud base.

More recently, Banfield et al. (1998), who make no attempt to retrieve particle sizes, assume a particle effective radius of 0.2 μm and retrieve optical depths from Galileo imaging data at a wavelength of 0.756 μm that cluster in the range ~ 1–4.5 (their Fig. 9). For comparison with the optical depths of ours and West et al.'s (at a mid-visible wavelength of 0.55 μm), we scale Banfield et al.'s τ by the ratio of extinction efficiencies at 0.55 to 0.756 μm for 0.2 μm particles (using their refractive index of 1.4), resulting in a mid-visible τ range of ~ 2–10. Hence, the West et al. (1986) and Banfield et al. (1998) results are effectively identical and are hereafter lumped together as "West et al."

Recall from Figure 3 that the condensate scale height retrievals of Carlson et al. (1994) are consistent with our baseline model for $f_{\rm rain}$ between ~ 1 and 3. This entire $f_{\rm rain}$ range for our baseline model (in which $\sigma_g = 2$) is seen in Figure 5*a* to overlap with the data reported by West et al. (1986). The overlap corresponds to $r_{\rm eff}$ ranging from ~ 13 to 35 μm. A narrower size distribution results in larger droplet effective radii and therefore smaller optical depths; for the monodisperse case, the data mutually overlap at $r_{\rm eff} \sim 30$ to 50 μm.

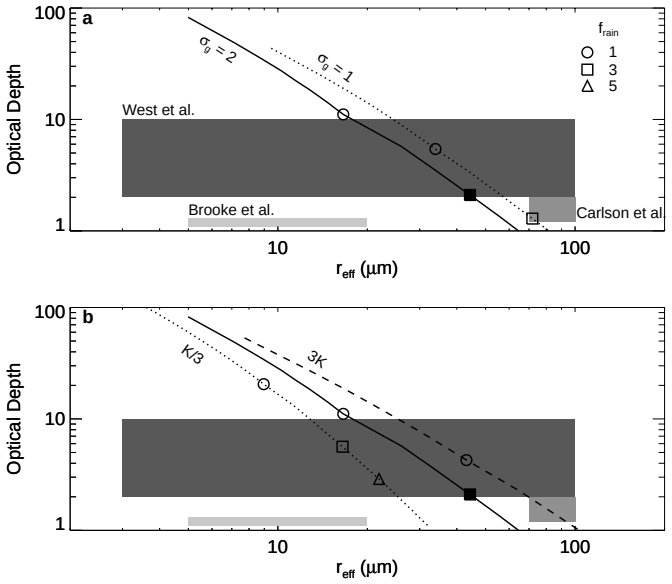

FIG. 5.—Condensate optical depth (for geometric scatterers) plotted as a function of particle effective radius ($r_{\rm eff}$) for the Jovian ammonia cloud. The darkest gray region corresponds to the range of observations given by West et al. (1986) (equivalent to Banfield et al. 1998, as described in the text), the medium gray region corresponds to the retrievals from *Voyager* IRIS 5–45 μm observations by Carlson et al. (1994), and the light gray region corresponds to retrievals from *ISO* 3 μm observations by Brooke et al. (1998). The lines correspond to variation of model results as $f_{\rm rain}$ ranges from 0.1 to 10, with results at $f_{\rm rain}$ of 1, 3, and 5 marked by symbols as denoted in (*a*). The particle effective radii correspond to opacity-weighted averages. The solid lines correspond to baseline values of (*a*) the width of the log-normal particle size distribution (σ_g) and (*b*) the eddy diffusion coefficient (K). The dotted line in (*a*) corresponds to a monodisperse particle size distribution; the dotted and dashed lines in (*b*) correspond, respectively, to dividing and multiplying K by a factor of 3. Filled-in squares denote model results using the complete baseline set of parameters.

Carlson et al. (1994) use *Voyager* IRIS spectra to retrieve cloud optical depths[3] and droplet sizes for the Northern Equatorial Belt "hot spots" (note that the infrared data are insensitive to the submicron particles reported by West et al. 1986). Their best-fit particle distribution is a mixture of small ($r_{\rm eff} = 3$ μm, $\tau = 0.16$) and larger ($r_{\rm eff} = 100$ μm, $\tau = 0.38$) particles, resulting in a combined $r_{\rm eff} = 72$ μm and $\tau = 0.54$. However, hot spots are anomalous features of reduced cloudiness associated with pronounced dynamical forcings (e.g., Showman & Ingersoll 1998), and our one-dimensional model is intended to represent horizontally averaged conditions, which would seem more comparable to the Equatorial and Northern Tropical Zones, where Carlson et al. retrieve τ of ~ 1.2 and 2, respectively. Carlson et al. do not present separate retrievals of droplet sizes for the zones, but do state that their optical depths are dominated by larger particles, which we interpret as an observed range of 70 μm $\leq r_{\rm eff} \leq$ 100 μm.

Given that our model results overlap with the entire range of the West et al. (1986) optical depths, which, in turn, do not overlap with those of Carlson et al. (1994), it should not be surprising that there is no mutual overlap between our baseline model results and the retrievals of τ and $r_{\rm eff}$ by Carlson et al. (1994). Although not shown in Figure 5, increasing the subcloud abundance enhances our model optical depths but does not influence the effective radii, suggesting the possibility of agreement with the Carlson et al. (1994) microphysical retrievals for $f_{\rm rain} > 4$. Such large values of $f_{\rm rain}$ are just barely ruled out by the Carlson et al. (1994) condensate scale heights (Fig. 3). Alternatively, multiplying our eddy diffusion coefficients by a factor of 3 results in larger particles and therefore reduced optical depths, which leads to overlap with the Carlson et al. (1994) retrievals for a range of $f_{\rm rain}$ between ~ 2 and 3 (Fig. 5*b*).

The above comparisons show that reasonable choices of model parameters produce agreement with observations of tropical Jovian ammonia clouds. The few unknown model parameters in our simple model are not uniquely constrained, befitting the incompleteness and uncertainty in the observations and the ambiguity in comparing a model for globally averaged clouds with measurements that resolve large-scale horizontal variability in the clouds. To compare our model with observations averaged over a wider area, we next consider measurements of the Jovian tropics obtained from Earth orbit.

Brooke et al. (1998) use a 3 μm *ISO* spectrum to retrieve microphysical properties of the Jovian ammonia cloud and find best fits for two possibilities: first, a monomodal distribution of 10 μm ammonia particles with a visible optical depth of 1.1; second, a bimodal distribution of 1 and 10 μm ammonia particles with an optical depth of 1.3 (equivalent to an effective radius of 7 μm). Both fits include an additional optical depth of 0.1 from gray particles. In their analysis, a fit for 10 μm particles indicates a superior fit in comparison to those for 1 and 30 μm particles, which we interpret as allowing a size range of 5 to 20 μm. Recalling from the discussion of Figure 3 that the Brooke et al. (1998) condensate scale height (a single value with no uncertainty) is consistent with $f_{\rm rain} = 2$. Figure 5*b* indicates that mutual consistency with the effective radii retrieved by Brooke et al. (1998) requires increasing the width of our size distributions and/or reducing our eddy diffusion coefficients. Simultaneously matching the Brooke et al. (1998) optical depths requires a substantial reduction of the subcloud ammonia abundance. However, the baseline ammonia abundance we use is reported by Brooke et al. (1998; as a single value with no uncertainty) to best fit their 3 μm spectrum. Hence, our calculations are evidently inconsistent with that baseline ammonia abundance and the combination of small particles and small optical depths retrieved by Brooke et al. (1998).

We have already noted the shortcoming that our model excludes the possibility of horizontal variability. For the case of modeling emitted radiative flux, this simplification will, of course, result in an underestimate at some wavelengths since any flux leaking out through the clearings between patchy clouds is not treated. Horizontal variability is also ignored in the retrievals of Brooke et al. (1998), which results in their underestimating cloud optical depth because of a plane-parallel albedo bias (e.g., Cahalan et al. 1994): the area-weighted albedo of a cloud deck calculated from a single column with an optical depth τ is always greater than the albedo averaged over a variety of columns with the same area-weighted average τ. Inverted for the Brooke et al. (1998) retrievals of optical depth from reflected spectra, this bias indicates that the optical depth from an area-weighted average radiance underestimates the area-weighted optical depth. Hence, the actual area-weighted optical depth is greater than that reported by Brooke et al. (1998) and closer to the optical depths calculated by our model. We are unable to quantify the magnitude of this error without reproducing their retrievals, which is beyond the scope of this study.

5. APPLICATIONS TO SUBSTELLAR ATMOSPHERES

5.1. *Vertical Cloud Structure*

We use our baseline model (Table 1) to calculate profiles of condensed water, silicate (as enstatite, $MgSiO_3$), and iron in theoretical atmospheres of brown dwarfs and a giant planet (see Fig. 6 for gravities and effective temperatures). The temperature profiles are calculated for cloud-free conditions (Marley 2000). The L dwarf–like atmosphere (Fig. 6*a*) is too warm for water to condense. Between 1 and 10 bars, within the convective region, the silicate and iron clouds are seen to overlap, suggesting the possibility of microphysical interactions between them, which are ignored by our model. The silicate particles in this case are about twice as large as the iron particles because the assumed density of a silicate particle is about half that of an iron particle (Appendix B).

Although the temperature profiles in Figure 6 were not calculated self-consistently to include the effects of clouds, it is clear that for objects near $T_{\rm eff} \sim 1500$ K, clouds are an important opacity source. The silicate and iron clouds in the L dwarf–like model (Fig. 6*a*) appear in the visible atmosphere and therefore play an important role in controlling opacity and the temperature structure of the atmosphere. Nevertheless, these clouds are confined to a relatively thin cloud deck, which does not reach the upper regions of the atmosphere as do condensates in the well-mixed profiles also shown. The cloud particles are also fairly large ($r_{\rm eff} \sim$ 40–80 μm) and will have a substantially different spectral opacity than smaller particles. The Lyon group (Chabrier et

[3] Carlson et al. (1994) report cloud optical depths for an assumed extinction efficiency of 1, whereas by treating cloud particles as geometric scatterers, we assume an extinction efficiency of 2. Hence, we multiply their optical depths by 2 for comparison with ours.

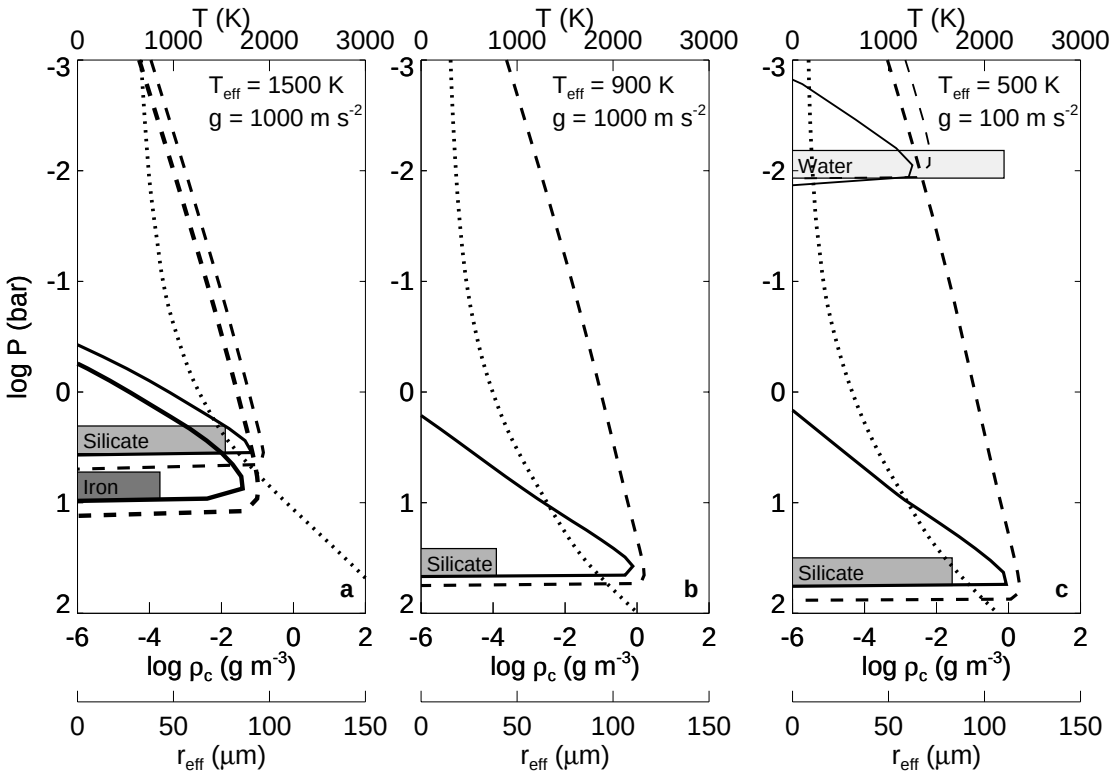

FIG. 6.—Profiles of temperature (*dotted curves*) and condensate mass concentration from baseline model (ρ_c, *solid curves*) in theoretical atmospheres of an (*a*) L dwarf, (*b*) T dwarf, and (*c*) extrasolar giant planet. Droplet effective radii at cloud base are shown as horizontal bars. Well-mixed clouds are shown as dashed curves. The theoretical temperature profiles are calculated for cloud-free conditions.

al. 2000) employs an "astrophysical dust" size distribution of submicron particles to model dust opacity in such atmospheres. The cloud model presented here, with larger particles confined to a discrete cloud deck, represents a substantial departure from the previous work. In a future publication, we will discuss the spectral and color properties of atmospheres with these new cloud models.

Figure 6*b* presents the cloud model applied to a T dwarf–like atmosphere with $T_{\rm eff} = 900$ K, which is again too warm for water to condense. (No iron cloud is shown in Figures 6*b* and 6*c* because the cloud base is below the bottom of the model domain.) Although the silicate cloud and the omitted iron cloud may be important to the atmospheric temperature structure, they no longer represent significant opacity sources to an observer.

The changing role of cloud opacity with effective temperature is more clearly shown in Figure 7, which illustrates the brightness temperature spectra of several radiative-equilibrium models for brown dwarf atmospheres as well as the atmospheric temperature range over which most of the cloud opacity is found. In a model with $T_{\rm eff} = 1800$ K (Fig. 7*a*), the silicate cloud deck forms in the model stratosphere and is relatively thin. Comparison of the solid and dotted curves, which, respectively, include and exclude silicate and iron cloud opacities, shows little difference between the two cases. Since the cloud optical depth is only a few tenths, flux is efficiently transported from levels deeper than the base of the cloud. The iron cloud (not shown) adds a few more tenths of optical depth. Hence, the clear and cloudy models are very similar. Such a model would be appropriate for an early-type L dwarf.

Figure 7*b* shows the results for a cooler atmosphere, with

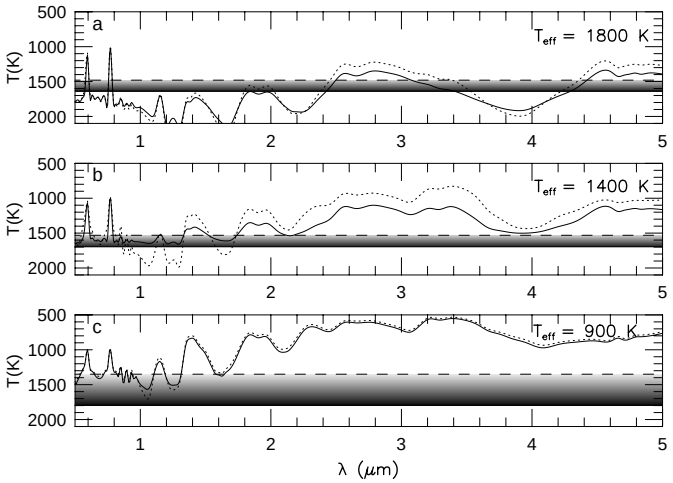

FIG. 7.—Brightness temperature as a function of wavelength for atmosphere models calculated self-consistently (Marley et al. 2001) to include (*solid*) or exclude (*dotted*) silicate and iron clouds. Brightness temperature increases downward to indicate increasing depth in the atmosphere. Clouds are calculated using the baseline model parameters. The solid straight line indicates the base of the silicate cloud, the dashed line denotes the level in the atmosphere at which column extinction optical depth reaches 0.1, and shading depicts the decrease in cloud extinction with altitude. Since cloud particle radius exceeds 10 μm in these models, the Mie extinction efficiency is not a strong function of wavelength over the range shown. Shown are models characteristic of (*a*) an early-type L dwarf with $T_{\rm eff} = 1800$ K, (*b*) a late-type L dwarf with $T_{\rm eff} = 1400$ K, and (*c*) a T dwarf with $T_{\rm eff} = 900$ K. All atmosphere models are for solar composition and gravitational acceleration of 1000 m s^{-2}, roughly appropriate for a 30 Jupiter-mass brown dwarf. Sodium and potassium lines, calculated using the theory of Burrows, Marley, & Sharp (2000), are prominent in the optical.

$T_{\rm eff} = 1400$ K, appropriate for a late L dwarf (Kirkpatrick et al. 1999; Stephens et al. 2001). Here the cloud is much more optically thick, and flux originates no deeper than the middle of the cloud layer. In the clear atmosphere, flux originates from deeper, hotter levels. As a result, the band depths of the cloudy model are shallower, a result shown for dusty M dwarfs by Jones & Tsuji (1997). Since flux is conserved for $T_{\rm eff}$ fixed, the cloudy model emits more flux beyond about 2 μm than the clear model. Regions of strong molecular absorption, including the depths of the water bands shortward of 2 μm as well as most of the 2 to 5 μm region evidence higher brightness temperatures in the cloudy case since the atmosphere above the cloud must warm to produce the same total emitted flux as in the cloud-free calculation. Regions of stronger molecular opacities are sensitive to these warmer temperatures higher in the atmosphere.

In Figure 7*c*, for which $T_{\rm eff} = 900$ K, the silicate cloud forms well below the region in which most flux originates and again the clear and cloudy models are similar. However, in the regions in which the molecular opacity is lowest, near 1.1 and 1.3 μm, flux originates from deeper regions in the clear atmosphere than for the cloudy case. As a result, the peak-to-trough variation in emitted flux is again somewhat smaller for the cloudy model. We note that clear atmosphere models for T dwarfs such as Gl 229B and GD 165B typically overpredict the water band depths (e.g., Marley et al. 1996; Allard et al. 1996; Tsuji et al. 1996; Saumon et al. 2000; Geballe et al. 2001) and suggest that the attenuation of flux by the top of the silicate cloud deck may be responsible for this effect.

Notably, these model atmospheres illustrate the origin of the curious change in infrared colors of the L and T dwarfs (e.g., Kirkpatrick et al. 1999; Martín et al. 1999; Fan et al. 2000). The cloud-free cases shown in the figure monotonically vary in $J-K$ from 1.39 to -0.17 from warmest to coolest. In contrast, the cloudy models initially become redder with falling $T_{\rm eff}$ (moving from 1.6 to 1.7) before they move to the blue ($J-K = 0.38$ for the case in Fig. 6*c*) when the silicate and iron clouds begin to disappear below optical depth unity in the gas. Thus our precipitating condensation cloud model qualitatively reproduces the color variation of the L and T dwarfs, which is consistent with previous arguments based on interpretation of spectra (Allard et al. 1996; Marley et al. 1996; Tsuji et al. 1996). In contrast, the pure chemical equilibrium model (Chabrier et al. 2000) predicts the presence of substantial dust opacity well to the top of the atmosphere, which is clearly excluded by the data. A more complete treatment of color changes will be given in a future study.

For the cooler atmosphere representative of a cool extrasolar giant planet (Fig. 6*c*), water condenses in the radiative region, in essence a stratospheric cloud. The ice particles are seen to be larger than the silicate particles, chiefly because of the lesser densities assumed for the individual ice particles. The reduced gravity in the atmosphere of the less massive extrasolar giant planet requires larger silicate particles to match the mean sedimentation velocity than does the more massive T dwarf. Note again that the well-mixed assumption produces a profoundly different vertical structure, in which the silicate cloud is so deep that it significantly overlaps the water cloud.

As did Marley et al. (1999), Sudarsky et al. (2000) have computed water cloud profiles in order to estimate extrasolar giant planet albedos. Sudarsky et al. (2000) essentially assume $f_{\rm rain} = 0$ and limit the cloud to be no more than 1 scale height thick. Such a model would be similar to the well-mixed water cloud in Figure 6*c* with a flat cloud top at $\sim 4 \times 10^{-3}$ bars.

The emergence of water clouds in substellar atmospheres with $T_{\rm eff}$ below about 500 K will reshape the vertical temperature profile and emergent spectra of these objects. Preliminary models computed with this cloud profile suggest that such cool objects will again move to the red in $J-K$ after the blueward excursion caused by the sinking of the silicate cloud below the visible atmosphere and the emergence of CH_4 as a dominant opacity source in the K band. Hence, the near-IR colors of very cool objects computed from cloud-free atmosphere models (e.g., Burrows et al. 1997) are likely to differ substantially from actual objects.

5.2. *Nonuniform Clouds*

Variable brightness in the I band has been detected for some L dwarfs by Bailer-Jones & Mundt (2001), who attribute the variability to evolution of dust clouds. They find some evidence that variability may be more common in later type L dwarfs. Although we do not model horizontally variable clouds, these observations are consistent with aspects of the model presented here. As clouds form in progressively cooler objects, they become more optically thick and form deeper within the convective region of the atmosphere. Thus global scale tropospheric weather patterns, as seen on Jupiter and predicted for brown dwarfs (Schubert & Zhang 2000), can more easily produce photometric variability since the turbulent motions are greater, making local clearings more likely, and enhancing the potential contrast between clear and cloudy air. Indeed, the Great Red Spot of Jupiter produces a photometric signal in both reflected sunlight and emitted thermal radiation (Gelino & Marley 2000).

Horizontally varying silicate clouds, even if not of the appropriate scale to produce a varying photometric signal, may play an important role in the transition from the dusty L dwarfs to the relatively cloud-free T dwarfs. The change in $J-K$ color from the latest red L dwarfs ($J-K \sim 2$) to the blue T dwarfs ($J-K \sim 0$) is quite abrupt. Four L8 dwarfs with known or estimated absolute magnitudes are only 1 mag brighter in the J band (Reid et al. 2001) than Gl 229B. Reid et al. argue that this implies the L8 dwarfs are only about 250 K warmer than Gl 229B. Even with the silicate cloud deck forming at progressively deeper levels with falling $T_{\rm eff}$, it may be difficult to account for such rapid color variation. In fact, the rapid transition may be a signature of horizontally varying clouds. Once tropospheric convective patterns begin to produce substantial horizontal variability, the flux from the more cloud-free regions will begin to dominate the total emitted flux, even if large fractions of the object are still cloudy. For example, Jupiter's 5 μm flux is dominated by the relatively cloud-free "hot spots" (Westphal et al. 1974) that typically cover about 1% of the surface area of the planet (Orton et al. 1996). Thus the apparent rapid change from cloudy L dwarfs to clear T dwarfs may be because of a gradual change in cloud coverage in the visible atmosphere, with the larger flux from the clear regions quickly dominating.

6. SUMMARY

We have developed a simple cloud model for substellar atmospheres that includes precipitation by condensate par-

ticles larger than that set by the convective velocity scale, which permits us to reproduce the properties retrieved from Jovian ammonia clouds. Effective precipitation also produces cloud profiles in theoretical brown dwarf and extrasolar giant planet atmospheres that are broadly consistent with observations.

As in the solar system, real clouds in the atmospheres of substellar objects will likely be neither uniform nor homogeneous; however, we hope that this model will provide a framework for evaluating the globally averaged role such clouds play in controlling the thermal radiative transfer and spectra of brown dwarfs and extrasolar giant planets.

We thank Sarah Beckmann for detecting anomalous behavior in an early version of the model. We also thank Robert West and Kevin Zahnle for providing helpful comments on the manuscript. M. S. M. acknowledges support from NASA grants NAG 58919 and NAG 59273 as well as NSF grants AST 9624878 and AST 0086288.

APPENDIX A

SATURATION VAPOR PRESSURES

For the saturation vapor pressure of ammonia (e_s, in dynes cm^{-2}), we fit the measurements tabulated in the CRC Handbook of Chemistry and Physics (Weast 1971) with

$$e_s(\mathrm{NH_3}) = \exp\left(10.53 - \frac{2161}{T} - \frac{86596}{T^2}\right), \tag{A1}$$

where the temperature is in K.

For the vapor pressure of water, we use the expressions of Buck (1981), over ice for $T < 273.16$ K, and over liquid water at greater temperatures:

$$e_s(\mathrm{H_2O,\ ice}) = 6111.5 \exp\left(\frac{23.036T_C - T_C^2/333.7}{T_C + 279.82}\right), \tag{A2a}$$

$$e_s(\mathrm{H_2O,\ liquid}) = 6112.1 \exp\left(\frac{18.729T_C - T_C^2/227.3}{T_C + 257.87}\right), \tag{A2b}$$

where T_C is the temperature in degrees Celsius. These expressions are unsuitable at $T > 1048$ K, leading to vapor pressures that decrease with increasing temperatures. Hence, at greater temperatures, we simply fix $e_s(\mathrm{H_2O}) = 6 \times 10^8$ dynes cm^{-2}, which is its value at $T = 1048$ K.

The vapor pressures for iron and enstatite are taken from Barshay & Lewis (1976). For iron below and above its melting point of 1800 K, we use, respectively,

$$e_s(\mathrm{Fe,\ solid}) = \exp\left(15.71 - \frac{47664}{T}\right), \tag{A3a}$$

$$e_s(\mathrm{Fe,\ liquid}) = \exp\left(9.86 - \frac{37120}{T}\right), \tag{A3b}$$

and for enstatite, we use

$$e_s(\mathrm{MgSiO_3}) = \exp\left(25.37 - \frac{58663}{T}\right). \tag{A4}$$

APPENDIX B

SEDIMENTATION VELOCITIES

Droplet terminal fallspeeds are calculated by first assuming viscous flow around spheres corrected for gas kinetic effects:

$$v_f = \frac{2}{9}\frac{\beta g r^2 \Delta\rho}{\eta}, \tag{B1}$$

where g is the gravitational acceleration, r is the droplet radius, and $\Delta\rho = \rho_p - \rho_a$ is the difference between the densities of the condensate and the atmosphere. The Cunningham slip factor, $\beta = (1 + 1.26N_{\mathrm{Kn}})$, accounts for gas kinetic effects, in which the Knudsen number (N_{Kn}) is the ratio of the molecular mean free path to the droplet radius. The dynamic viscosity of the

atmosphere is given by Rosner (2000):

$$\eta = \frac{5}{16}\frac{\sqrt{\pi m k_B T}}{\pi d^2}\frac{(k_B T/\epsilon)^{0.16}}{1.22}, \tag{B2}$$

where d is the molecular diameter and ϵ is the depth of the Lennard-Jones potential well for the atmosphere (2.827×10^{-8} cm and $59.7 k_B$ K, respectively, for H_2) and k_B is the Boltzmann constant.

For turbulent flow, at Reynolds numbers ($N_{Re} = 2r\rho_a v_f/\eta$) between 1 and 1000, we use a standard trick to solve the drag problem. Noting that $C_d N_{Re}^2 = 32\rho_a g r^3 \Delta\rho/3\eta^2$ is independent of fall velocity, we fit $y = \log(N_{Re})$ as a function of $x = \log(C_d N_{Re}^2)$ to the following data: at $N_{Re} = 1$, we assume viscous flow, with $C_d = 24$; for intermediate Reynolds numbers, we use the data for rigid spheres from Table 10-1 of Pruppacher & Klett (1978); and at $N_{Re} = 1000$, we assume an asymptote of $C_d = 0.45$. This asymptote is appropriate to moderately oblate spheroids (Fig. 10-36 in Pruppacher & Klett 1978), which are more appropriate to unknown condensates than the extreme case of smooth spheres. Our fit to the data is $y = 0.8x - 0.01x^2$, which allows us to evaluate the droplet terminal fall velocity from N_{Re}.

At Reynolds numbers greater than 1000, we assume the drag coefficient is fixed at its asymptotic value ($C_d = 0.45$), which leads to

$$v_f = \beta\sqrt{\frac{8gr\Delta\rho}{3C_d\rho_a}}. \tag{B3}$$

We assume rigid particles and thereby ignore breakup, for instance, by liquid droplets caused by hydrodynamic instability. For the density of ammonia ice particles, we use 0.84 g cm^{-3} (Manzhelii & Tolkachev 1964); for water, we use 0.93 g cm^{-3} (corresponding to ice at a temperature of 200 K, using eq. [4-17] from Pruppacher & Klett 1978); and for enstatite and iron, we use 3.2 and 7.9 g cm^{-3}, respectively (Table 1.18 of Lodders & Fegley 1998).

REFERENCES

Ackerman, A. S., Toon, O. B., & Hobbs, P. V. 1993, Science, 262, 226
Ackerman, A. S., Toon, O. B., Stevens, D. E., Heymsfield, A. J., Ramanathan, V., & Welton, E. J. 2000a, Science, 288, 1042
Ackerman, A. S., Toon, O. B., Taylor, J. P., Johnson, D. W., Hobbs, P. V., & Ferek, R. J. 2000b, J. Atmos. Sci., 57, 2684
Allard, F., Hauschildt, P. H., Baraffe, I., & Chabrier, G. 1996, ApJ, 465, L123
Bailer-Jones, C. A. L., & Mundt, R. 2001, A&A, 367, 218
Banfield, D., Gierasch, P. J., Bell, M., Ustinov, E., Ingersoll, A. P., Vasavada, A. R., West, R. A., & Belton, M. J. S. 1998, Icarus, 135, 230
Barshay, S. S., & Lewis, J. S. 1976, ARA&A, 14, 81
Basri, G., Mohanty, S., Allard, F., Hauschildt, P. H., Delfosse, X., Martín, E. L., Forveille, T., & Goldman, B. 2000, ApJ, 538, 363
Brooke, T. Y., Knacke, R. F., Encrenaz, Th., Drossart, P., Crisp, D., & Feuchtgruber, H. 1998, Icarus, 136, 1
Buck, A. L. 1981, J. Appl. Meteor., 20, 1527
Burrows, A., et al. 1997, ApJ, 491, 856
Burrows, A., Marley, M. S., & Sharp, C. M. 2000, ApJ, 531, 438
Cahalan, R. F., Ridgeway, W., Wiscombe, W. J., Bell, T. L., & Snider, J. B. 1994, J. Atmos. Sci., 51, 2434
Carlson, B. E., Lacis, A. A., & Rossow, W. B. 1993, J. Geophys. Res., 98, 5251
Carlson, B. E., Lacis, A. A., & Rossow, W. B. 1994, J. Geophys. Res., 99, 14623
Carlson, B. E., Rossow, W. B., & Orton, G. S. 1988, J. Atmos. Sci., 45, 2066
Chabrier, G., Baraffe, I., Allard, F. & Hauschildt, P. 2000, ApJ, 542, 464
Fan, X., et al. 2000, AJ, 119, 928
Fegley, B. J., & Lodders, K. 1994, Icarus, 110, 117
Geballe, T., Saumon, D., Leggett, S., Knapp, G., Marley, M., & Lodders, K. 2001, ApJ, 556, 373
Gelino, C., & Marley, M. 2000, in ASP Conf. Ser. 212, From Giant Planets to Cool Stars, ed. C. A. Griffith & M. S. Marley (San Francisco: ASP), 322
Gierasch, P. J., & Conrath, B. J. 1985, in Recent Advances in Planetary Meteorology, ed. G. E. Hunt (New York: Cambridge Univ. Press), 121
Jensen, E. J., et al. 2000, J. Geophys. Res., in press
Jones, H. R. A., & Tsuji, T. 1997, ApJ, 480, L39
Kirkpatrick, J. D., et al. 1999, ApJ, 519, 802
Kunde, V., et al. 1982, ApJ, 263, 443
Leggett, S. K., Allard, F., & Hauschildt, P. H. 1998, ApJ, 509, 836
Leggett, S. K., Toomey, D. W., Geballe, T. R., & Brown, R. H. 1999, ApJ, 517, L139
Lewis, J. S. 1969, Icarus, 10, 365
Lindal, G. F., et al. 1981, J. Geophys. Res., 86, 8721
Lindzen, R. S. 1981, J. Atmos. Sci., 86, 9707
Lodders, K., & Fegley, B., Jr. 1998, The Planetary Scientist's Companion (New York: Oxford)
Lunine, J. I., Hubbard, W. B., Burrows, A., Wang, Y.-P., & Garlow, K. 1989, ApJ, 338, 314
Manzhelii, V. G., & Tolkachev, A. M. 1964, Sov. Phys. Solid State, 5, 2506
Marley, M. S. 2000, in ASP Conf. Ser. 212, From Giant Planets to Cool Stars, ed. C. A. Griffith & M. S. Marley (San Francisco: ASP), 152
Marley, M. S., Gelino, C., Stephens, D., Lunine, J. I., & Freedman, R. 1999, ApJ, 513, 879
Marley, M. S., Saumon, D., Guillot, T., Freedman, R. S., Hubbard, W. B., Burrows, A., & Lunine, J. I. 1996, Science, 272, 1919
Marley, M. S., Seager, S., Saumon, D., Lodder, K., Ackerman, A. S., & Freedman, R. 2001, ApJ, submitted
Martín, E. L., Delfosse, X., Basri, G., Goldman, B., Forveille, T., & Zapatero Osorio, M. R. 1999, AJ, 118, 2466
Nicholls, S. 1984, Q. J. R. Meteorol. Soc., 112, 431
Orton, G., et al. 1996, Science, 272, 839
Prinn, R. G. 1974, J. Atmos. Sci., 31, 1691
Prinn, R. G., & Olaguer, E. P. 1981, J. Geophys. Res., 86, 9895
Pruppacher, H. R., & Klett, J. D. 1978, Microphysics of Clouds and Precipitation (Dordrecht: Kluwer)
Reid, I. N., Gizis, J. E., Kirkpatrick, J. D., & Koerner, D. W. 2001, AJ, 121, 489
Rosner, D. E. 2000, Transport Processes in Chemically Reacting Flow Systems (Dover: Mineola)
Rossow, W. B. 1978, Icarus, 36, 1
Saumon, D., Geballe, T. R., Leggett, S. K., Marley, M. S., Freedman, R. S., Lodders, K., Fegley, B. & Sengupta, S. K. 2000, ApJ, 541, 374
Schubert, G., & Zhang K. 2000, in ASP Conf. Ser. 212, From Giant Planets to Cool Stars, ed. C. A. Griffith & M. S. Marley (San Francisco: ASP), 210
Showman, A. P. D., & Ingersoll, A. P. 1998, Icarus, 132, 205
Stephens, D., Marley, M., Noll, K., & Chanover, N. 2001, ApJ, in press
Stevens, B., Cotton, W. R., Feingold, G., Moeng, C.-H. 1998, J. Atmos. Sci., 55, 3616
Sudarsky, D., Burrows, A., & Pinto, P. 2000, ApJ, 538, 885
Taylor, J. P., & Ackerman, A. S. 1999, Q. J. R. Meteorol. Soc., 125, 2643
Toon, O. B., McKay, C. P., Courtin, R., & Ackerman, T. P. 1988, Icarus, 75, 255
Tsuji, T., Ohnaka, K., Aoki, W., & Nakajima, T. 1996, A&A, 308, L29
Tsvetanov, Z. I., et al. 2000, ApJ, 531, L61
Weidenschilling, S. J., & Lewis, J. S. 1973, Icarus, 20, 465
Weast, R. C., ed. 1971, Handbook of Chemistry and Physics (52d ed.; Boca Raton: CRC)
West, R. A., Strobel, D. F., & Tomasko, M. G. 1986, Icarus, 65, 161
Westphal, J. A., Matthews, K., & Terrile, R. J. 1974, ApJ, 188, L111